Quantum cutting by cooperative energy transfer in $Yb_xY_{1-x}PO_4:Tb^{3+}$

P. Vergeer,* T. J. H. Vlugt, M. H. F. Kox, M. I. den Hertog, J. P. J. M. van der Eerden, and A. Meijerink
Condensed Matter and Interfaces, Debye Institute, Utrecht University, P.O. Box 80000, 3508 TA Utrecht, The Netherlands
(Received 10 May 2004; revised manuscript received 24 September 2004; published 31 January 2005)

We present experimental evidence for cooperative energy transfer from Tb^{3+} to two Yb^{3+} ions and a determination of the energy-transfer rate. Energy transfer from Tb^{3+} to Yb^{3+} was investigated by luminescence measurements on $(Yb_xY_{1-x})PO_4$ doped with 1% Tb^{3+}. Time-resolved luminescence experiments were analyzed using Monte Carlo simulations based on theories for phonon-assisted, cooperative, and accretive energy transfer. The luminescence decay curves of the $^5D_4$ emission from Tb^{3+} show an excellent agreement with simulations based on cooperative energy transfer via dipole-dipole interaction, while a phonon-assisted or an accretive energy-transfer mechanism cannot explain the experimental results. The energy-transfer rate to two nearest-neighbor Yb^{3+} ions is 0.26 ms^{-1}. This corresponds to an upper limit of the energy-transfer efficiency of 88% in $YbPO_4$. Application of cooperative energy transfer has prospects for increasing the energy efficiency of crystalline Si solar cells by photon doubling of the high energy part of the solar spectrum.

DOI: 10.1103/PhysRevB.71.014119 PACS number(s): 32.70.Cs, 32.80.Wr, 33.50.Hv, 42.50.Fx

I. INTRODUCTION

The recent discovery of visible quantum cutting phosphors[1,2] has been an exciting development in the search for luminescent materials with a high energy efficiency. In luminescent devices such as fluorescent tubes or plasma display panels, the phosphors used nowadays convert one UV photon into one visible photon by dissipating roughly 50% of the absorbed energy into heat. The efficiency gain in quantum cutting materials is based on the principle that a quantum cutting phosphor is able to emit two visible photons for every (vacuum) ultraviolet photon absorbed. The excitation energy is divided over the two photons, leading to the necessary redshift of the absorbed radiation without losing energy efficiency.

Quantum cutting materials may also be applied in solar cells.[3] If conversion of one UV/VIS photon into two IR photons is realized, energy losses by thermalization of electron-hole pairs are minimized. The most widely used solar cells are based on crystalline Si. The development of solar cells would greatly benefit from a quantum cutting phosphor with the energy of its emission located just above the band gap of Si.

Research on quantum cutting systems started on single ions capable of a cascade emission such as Pr^{3+},[4,5] Tm^{3+},[6] and Gd^{3+}.[7] Recently, the focus has shifted to combinations of two ions, where the energy of the donor ion is transferred stepwise to two acceptor ions. This process is generally known as downconversion. A well-known example is the $Gd^{3+}-Eu^{3+}$ couple,[1] where for every vacuum ultraviolet (VUV, $\lambda < 200$ nm) photon absorbed by Gd^{3+}, two red photons are emitted by different Eu^{3+} centers. Another example is the combination $Gd^{3+}-Tb^{3+}-Er^{3+}$.[2] In both systems, VUV radiation is downconverted to visible radiation.

Theories for predicting energy-transfer rates (including down- and upconversion) were developed in the late 1940s and 1950s by Förster[8] and Dexter.[9] These theories are based on different models for the interaction between donor and acceptor centers, viz. dipole-dipole interaction versus exchange interaction through wave-function overlap. These have in common that the donor and the acceptor transitions should be resonant as the spectral overlap integral relates the energy-transfer rate to the density of acceptor and donor states at a resonant frequency. Therefore, to facilitate first-order energy transfer, the emission spectrum of the donor should overlap with the excitation spectrum of the acceptor. The two quantum-cutting phosphors mentioned above are based on this principle. Splitting of the energy is reached by population of an intermediate energy level of the donor.

If overlap between donor emission and acceptor absorption is absent, second-order downconversion may become the dominant relaxation process (competing with spontaneous emission). In this process a donor excites two acceptors simultaneously. The resonance condition is fulfilled if the sum of the energy of the absorption transitions of the two acceptor centers equals the energy of the emission of the donor.

This cooperative sensitization process was predicted in 1957 by Dexter[9] but only recently Basiev *et al.* observed the occurrence of second-order downconversion[10] by measuring the enhancement of the Nd^{3+} $^4F_{3/2} \rightarrow {}^4I_{15/2}$ decay rate upon increasing the Ce^{3+} concentration in the compound $La_{1-x}Ce_xF_3:Nd^{3+}$ 0.3%. This enhancement was attributed to second-order downconversion from the Nd^{3+} $^4F_{3/2}$ level exciting two Ce^{3+} ions to their $^2F_{7/2}$ level. Unfortunately, the Ce^{3+} $^2F_{7/2} \rightarrow {}^2F_{5/2}$ emission, in the infrared ($\sim$5000 nm), was not detected and therefore direct proof of energy transfer from Nd^{3+} to Ce^{3+} was not obtained. In later papers Basiev *et al.* addressed simulations and theory on second-order energy-transfer processes,[11,12] but no comparison to experiments was made.

A promising system to study second-order energy-transfer processes is the combination of one Tb^{3+} and two Yb^{3+} ions: the Tb^{3+} $^5D_4 \rightarrow {}^7F_6$ transition is located at approximately twice the energy of the Yb^{3+} $^2F_{7/2} \rightarrow {}^2F_{5/2}$ transition and Yb^{3+} has no other levels up to the UV region (see Fig. 1). Moreover, the $^2F_{5/2} \rightarrow {}^2F_{7/2}$ emission is situated around 1000 nm, just above the band edge of crystalline Si.

Previous studies of Tb–Yb compounds have focused on the experimental observation of upconversion.[13–25] When these compounds are exposed to infrared radiation around 1000 nm, Yb^{3+} ions act as absorption centers. After an up-

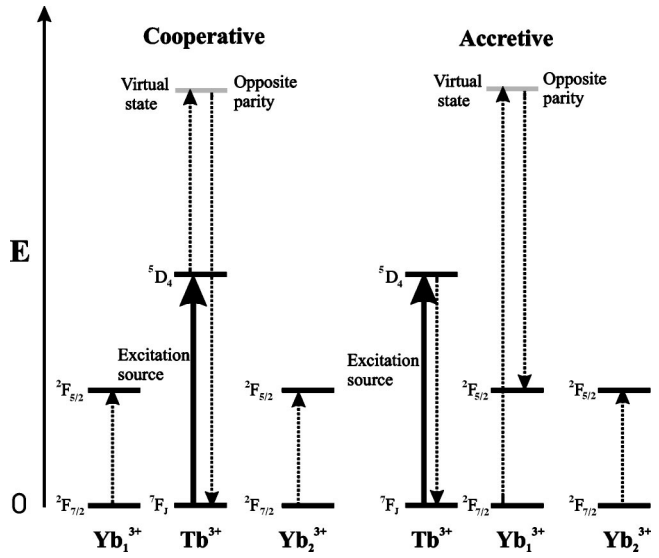

FIG. 1. Schematic representation of the cooperative and accretive pathways for energy transfer from Tb^{3+} to Yb^{3+}. The bold arrows indicate excitation of Tb^{3+} into the $^5D_4$ state, after which energy transfer may occur. The energy transfer processes are depicted by the dotted lines. In both mechanisms a virtual state is involved. For the cooperative mechanism, the virtual state is located on Tb^{3+}. For the accretive mechanism, the virtual state is located on Yb^{3+}. Since the total amount of energy is unchanged after the energy transfer, the resonance condition implies that the transition energy of Tb^{3+} balances the sum of the transition energies of the Yb^{3+} ions.

conversion process, green Tb^{3+} luminescence was observed. If energy transfer by a second-order process is responsible for the upconverted luminescence, downconversion should occur as well. In some studies mentioned above, this becomes apparent by an increased decay rate of the upconverted luminescence compared to directly excited Tb^{3+} luminescence.[13–15,21,22,24] However, in analyzing transient luminescence curves, the downconversion probability has often been neglected. Studies that do consider downconversion mention two possibilities for the decay mechanism: second-order energy transfer and phonon-assisted energy transfer.[20,22,23] However, downconversion in the Tb–Yb system by either one of these mechanisms has never been established experimentally.

The purpose of this paper is to study second-order downconversion in Tb–Yb compounds and to elucidate its efficiency and energy-transfer mechanism. Energy transfer in powders of $Yb_xY_{1-x}PO_4$ doped with 1% Tb^{3+} is studied by emission, excitation, and time resolved luminescence measurements. The time resolved luminescence measurements are compared with theories for phonon-assisted energy transfer[26] and second-order downconversion by simulations using Monte Carlo methods and exact calculations. According to Auzel[16] and Andrews and Jenkins[27] second-order downconversion can occur through a cooperative and an accretive mechanism. The present analysis shows that the cooperative dipole-dipole mechanism gives an excellent agreement between theory and experiment. Energy transfer via the accretive or the phonon-assisted mechanism cannot explain the experimental observations.

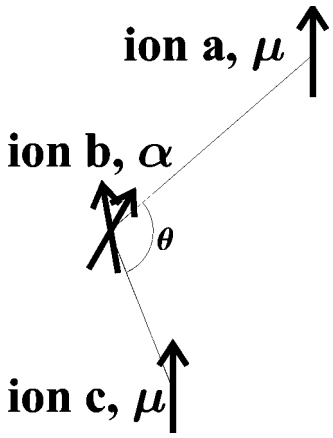

FIG. 2. Orientational dependence of three-ion energy transfer. The arrows denote transition dipole moments $\boldsymbol{\mu}$. Since the matrix $\boldsymbol{\alpha}$ [Eq. (3)] consists of products of two transition dipole moments it is denoted by two arrows. The three-body energy-transfer rate, viz. Eq. (6), shows a weak dependence on the angle θ between the lines connecting ion-pairs *ab* and *bc*.

The energy-transfer efficiency is shown to be 88% for $YbPO_4$:Tb^{3+} 1%. This means that 88 out of 100 Tb^{3+} ions each transfer their energy to two Yb^{3+} ions. This makes, in principle, a quantum efficiency of 188% possible, although this is not observed due to concentration quenching at high Yb^{3+} doping concentrations. The relatively high transfer efficiency shows the potential for Tb–Yb based quantum cutting phosphors in increasing the energy efficiency of crystalline Si-based solar cells by downconversion of the higher energy part of the solar spectrum.

II. THEORY

This section reviews possible mechanisms for energy transfer, with emphasis on the interion distance and orientation dependence. For three energy-transfer mechanisms, the cooperative, accretive,[16,27] and the phonon-assisted[26] mechanism, energy-transfer rates will be obtained that are used to compute ensemble averaged decay curves for the donor luminescence in the Monte Carlo simulations and in the analytical solutions. We will assume orientationally averaged transition dipole moments. For the second-order energy-transfer processes, this appears to result in a minor dependence of the transfer rate to the interion orientation (as defined by the angle θ in Fig. 2).

Auzel[16] mentions two mechanisms for second-order energy transfer: a cooperative and an accretive mechanism (see Fig. 1). After excitation of the donor (Tb^{3+} $^7F_6 \rightarrow {}^5D_4$), both mechanisms require polarization induced via a virtual state of opposite parity. For the cooperative pathway, the virtual state is located on the donor (Tb^{3+}) ion and this ion acts twice as a donor of energy. For the accretive pathway, the virtual state is located on one of the acceptor (Yb^{3+}) ions. The latter accepts energy from the donor ion, after which part of the energy is transferred to the second acceptor ion.

For both of these mechanisms, Andrews and Jenkins[27] have calculated the matrix element M needed as input in

Fermi's golden rule to determine the energy-transfer rate,

$$\gamma_{\mathrm{tr}} = \frac{2\pi}{\hbar}|M|^2\rho. \tag{1}$$

For a specific pathway, M has the form (see Fig. 2)

$$M = \boldsymbol{\mu}^a \cdot \mathbf{V}^{ab} \cdot \boldsymbol{\alpha}^b \cdot \mathbf{V}^{bc} \cdot \boldsymbol{\mu}^c. \tag{2}$$

Here, the superscripts denote the ions involved. For the cooperative process, a and c denote Yb^{3+} ions and b denotes a Tb^{3+} ion. For an accretive process, a denotes a Tb^{3+} ion and b and c denote Yb^{3+} ions. The vector $\boldsymbol{\mu}^k$ is the transition dipole moment for a transition on ion k and $\boldsymbol{\alpha}^b$ is the two-photon interaction tensor, describing the transition on ion b, via a virtual state. The element ij of $\boldsymbol{\alpha}^b$ is given by

$$\alpha_{ij}^b(\mp\omega_a, \mp\omega_c) = \sum_{\xi}\left(\frac{\mu_i^{2\xi b}\mu_j^{\xi 1 b}}{E_{\xi 1} \pm \hbar\omega_a} + \frac{\mu_i^{\xi 1 b}\mu_j^{2\xi b}}{E_{\xi 1} \pm \hbar\omega_c}\right), \tag{3}$$

where the $\mp$ are chosen with respect to the flow of energy in the system[27] and i and j denote the x, y, or z direction. The angular frequencies for the transitions on ions a and c are given by ω_a and ω_b, respectively. The sum runs over all virtual states ξ of ion b. The indices 1 and 2, respectively, denote the initial and the final state of ion b. $E_{\xi 1}$ is the energy of the virtual state with respect to the initial state. When including line broadening due to the finite lifetimes, $E_{\xi 1}$ should be treated as a complex quantity. However, the angular frequencies of transitions to opposite parity states on Tb^{3+} or Yb^{3+} are typically 10^{16} rad/s (in the UV spectral region), so that line broadening is small for lifetimes larger then 10^{-15} s. Therefore we treat $E_{\xi 1}$ as a real quantity.

The second-rank tensor $\mathbf{V}^{ab}$ contains the distance and the interion orientation dependence. In our analysis, the elements ij of $\mathbf{V}^{ab}$ have been simplified to the Förster analogy. This is justified for interion distances r much shorter than the wavelength of light ($r \ll 2\pi c/n\omega$, with n the refractive index of the material and ω the angular frequency associated with the energy of the transition). This leads to

$$V_{ij}^{ab} = \frac{1}{n^2}\left(\frac{n^2+2}{3}\right)^2 \frac{1}{4\pi\varepsilon_0 {r_{ab}}^3} v_{ij}^{ab}, \tag{4}$$

where r_{ab} is the distance between ions a and b, and v_{ij}^{ab} is the matrix element $\delta_{ij} - \hat{r}_i\hat{r}_j$. The quantities $\hat{r}_i$ and $\hat{r}_j$ are the x, y, or z components of the unit vector connecting the two ions.

In Eq. (1), $|M|^2$ consists of contributions from cooperative processes, accretive processes, and mixtures of the two. Given the nature of the interacting ions, either the cooperative or the accretive process is expected to dominate. In order to obtain the transfer rate for these processes, three assumptions are made. First, all ions of the same species are assumed to be energetically equivalent, i.e., line shapes are homogeneously broadened. This allows us to separate the spatial dependence from the spectral part. For the cooperative process this leads to

$$\gamma_{\mathrm{coop}} = \frac{2\pi}{\hbar}\frac{1}{n^8}\left(\frac{n^2+2}{3}\right)^8 \frac{\rho}{(4\pi\varepsilon_0)^4} \times \sum_a \sum_{c>a} \frac{\left|\boldsymbol{\mu}^a \cdot \mathbf{v}^{a\mathrm{Tb}} \cdot \boldsymbol{\alpha}^{\mathrm{Tb}} \cdot \mathbf{v}^{\mathrm{Tb}c} \cdot \boldsymbol{\mu}^c\right|^2}{r_{a\mathrm{Tb}}^6 r_{\mathrm{Tb}c}^6}. \tag{5}$$

Here, a and c run over all Yb^{3+} positions in the lattice. Second, in the analysis of first-order energy transfer the transition dipole moments are often treated as randomly oriented.[28] In analogy, we will do this for the dipole moments in Eq. (5). However, we treat the products of dipole moments in α^b [Eq. (3)] as fully correlated since a virtual state ξ couples the dipole moment pair. Transitions involving different virtual states ξ are treated as uncorrelated, since the ($4f$ configuration) levels 2 and 1 contain many different M_J's which couple to different ξ. Third, we assume that the transitions to and from virtual states are also uncorrelated with respect to their transition frequency.

The three assumptions above allow one to average over all orientations of the transition dipole moments. We will perform the orientational averaging assuming classical angular distributions of the transition dipole moments. Relying on the quantum mechanical analog would involve summing over all virtual states explicitly and taking all substates $|J, M_J\rangle$ of the levels involved on the Tb^{3+} and the Yb^{3+} ions into account. This entails a tremendous effort and is beyond the scope of this work.

After substitution of $\boldsymbol{\alpha}^{\mathrm{Tb}}$ by Eq. (3) one obtains for the orientational average,

$$\left\langle\left|\boldsymbol{\mu}^a \cdot \mathbf{v}^{a\mathrm{Tb}} \cdot \boldsymbol{\alpha}^{\mathrm{Tb}} \cdot \mathbf{v}^{\mathrm{Tb}c} \cdot \boldsymbol{\mu}^c\right|^2\right\rangle = \frac{4}{9}(3+\cos 2\theta)\sum_{\xi}\left[\left(\mu^a\mu^{2\xi\mathrm{Tb}}\mu^{\xi 1\mathrm{Tb}}\mu^c\right)^2 \times\left(\frac{1}{(E_{\xi 1} \pm \hbar\omega_a)} + \frac{1}{(E_{\xi 1} \pm \hbar\omega_c)}\right)^2\right], \tag{6}$$

where $\langle\ \rangle$ means orientational averaging over all dipole moments. The average depends on the angle θ between the pairs ab and bc (see Fig. 2). The contribution of the angular dependent part is at maximum 25%. The summation over different triples would even lower the angular dependant contribution. Therefore, in the Monte Carlo simulations we neglect the angular dependence and approximate the cooperative energy-transfer rate by

$$\gamma_{\mathrm{coop}} = C_{\mathrm{coop}}\sum_a \sum_{c>a} \frac{1}{r_{a\mathrm{Tb}}^6 r_{\mathrm{Tb}c}^6}, \tag{7}$$

which is independent of θ. The constant C_{coop} will be fitted in the Monte Carlo simulations and the analytical solutions that describe the time dependence of the donor emission intensity.

The energy-transfer rate of the accretive energy-transfer process can be treated analogously. However, since there are two accretive pathways, one where the energy is accrued at b and the other where the energy is accrued at c, the matrix element M for the accretive pathway consists of the sum of

two contributions. Upon evaluation of Eq. (1) one may note that quantum interference terms vanish in the orientational averaging. This leads to

$$\gamma_{\mathrm{accr}} = C_{\mathrm{accr}} \sum_{b} \sum_{c>b} \left(\frac{1}{r_{\mathrm{Tb}b}^6 r_{bc}^6} + \frac{1}{r_{\mathrm{Tb}c}^6 r_{bc}^6} \right), \tag{8}$$

where b and c run over all Yb^{3+} positions in the lattice. Again, C_{accr} will be fitted in the Monte Carlo simulations.

The third energy-transfer mechanism, phonon-assisted energy transfer, is an energy-transfer process in which the energy difference between the transition on the donor (Tb^{3+}) and the transition on the acceptor (Yb^{3+}) is dissipated by multiphonon emission. The transfer rate $\gamma_{\mathrm{pa}}(\Delta E)$ for a process creating phonons is given by[26]

$$\gamma_{\mathrm{pa}}(\Delta E) = (n_{\mathrm{ph}} + 1)^p \gamma_{\mathrm{tr}}(\Delta E = 0) \exp(-\kappa \Delta E). \tag{9}$$

Here, ΔE is the energy difference between the energy of the donor and acceptor transitions, n_{ph} is the phonon occupation number, and p the minimum number of available phonons required to bridge the energy gap ΔE. The energy-transfer rate γ_{tr} is the (first-order) energy-transfer rate when energy mismatches are absent. The electron-phonon coupling is described by κ. For an dipole-dipole energy-transfer mechanism, orientational averaging over the transition dipole moments yields $\frac{2}{3}$, so that the transfer rate γ_{pa} can be written as

$$\gamma_{\mathrm{pa}} = C_{\mathrm{pa}} \sum_{a} \frac{1}{r_{\mathrm{Tb}a}^6}, \tag{10}$$

where the sum runs over all Yb^{3+} ions in the lattice. The parameter C_{pa} will be fitted in the Monte Carlo simulations.

III. EXPERIMENT

A. Sample preparation

Powder samples of $Yb_xY_{0.99-x}Tb_{0.01}PO_4$ were prepared by common solid-state methods. Stock solutions of Yb^{3+} and Y^{3+}, both containing 1% of Tb^{3+}, were prepared by dissolving rare earth (RE) oxides in concentrated hydrochloric acid. The purity of the oxides, as labeled by the suppliers, was 4N (Y_2O_3) or 5N (Tb_4O_7) and (Yb_2O_3)). A solution with the desired ratio of Y^{3+} to Yb^{3+} was obtained by combining appropriate amounts of the stock solutions. The rare earth ions in the mixed solution were subsequently precipitated by adding a solution with an excess of oxalic acid. The precipitate was washed thoroughly to eliminate chloride ions. Heating the compound to 1050 °C under an oxygen atmosphere converted the oxalates to oxides. The powder obtained was mixed with diammoniumphosphate (10 mol % excess) and fired again at 1350 °C under a 1:3 $H_2:N_2$ atmosphere. The white powder obtained was checked for phase purity with x-ray diffraction and found to be single-phase zircon $REPO_4$. In this way, samples of $Yb_xY_{0.99-x}PO_4:Tb^{3+}$ 1% were prepared with $x=0$, 0.05, 0.15, 0.25, 0.50, 0.75, and 0.99.

B. Optical measurements

Emission and excitation measurements were performed using a SPEX DM3000F spectrofluorometer with a 450 W Xe-lamp as the excitation source. The excitation light was dispersed by a double-grating 0.220 m SPEX 1680-monochromator (1200 l/mm) blazed at 300 nm. The light emitted by the sample was focused on a fiber guiding the light to a monochromator where the emission light was dispersed by a 150 l/mm grating (Scientific Spectra Pro) blazed at 500 nm with 0.300 m focal length and detected using a Princeton Instruments 300i charge coupled device camera. Tb^{3+} $^5D_4 \rightarrow {}^7F_J$ emission was rejected by the use of appropriate filters. Emission spectra were not corrected for instrumental response. Therefore, the intensity in the IR region of the spectra is underestimated by a factor of ~15.

Time resolved measurements with an excitation wavelength of 489.6 nm were performed with the use of a Lamba Physic LPD3000 tunable dye laser filled with a Coumarine 307 dye solution. It is pumped by a Lambda Physic LPX100 excimer (XeCl) laser. The typical pulse width of this setup is ~20 ns.[29] Time resolved measurements with an excitation wavelength of 193 nm were performed using an excimer laser (TuiLaser) filled with an ArF gas mixture as the excitation source. The pulse duration of this laser is typically 10 ns. Emission of 544 nm was detected using a Jobin Yvon Triax 550 spectrometer equipped with a Hamamatsu R928 PMT and emission around 1000 nm was detected using a 780 nm cutoff filter in combination with a Si diode. The signal was monitored as a function of time using a Tektronix 2440 digital oscilloscope. .

In some cases, saturation effects occurred at short time intervals after the excitation pulse. For comparison with simulations and analytical calculations of the time dependence of the emission intensity, the maxima of the experimentally obtained decay curves were normalized and, if necessary, the simulated curves were multiplied by ~1.2 in order to correct for the short-time saturation. All measurements were performed at room temperature.

C. Monte Carlo simulations

For several Yb^{3+} concentrations in $Yb_xY_{1-x}PO_4:Tb^{3+}$ 1% the time resolved Tb^{3+} $^5D_4 \rightarrow {}^7F_J$ luminescence was simulated using conventional Monte Carlo techniques.[30–32] The following scheme was used for the simulations.

First, a discrete atom model was created using the YPO_4 unit cell as input.[33] The structure of YPO_4 is tetragonal with $a=b=6.882$ Å and $c=6.020$ Å and four RE ions per unit cell. The RE^{3+} site has D_{2d} symmetry.[34] The size of the simulation box was 5^3 unit cells (500 RE atoms) and periodic boundary conditions were imposed. This means that we considered all interactions up to 15.05 Å. Second, the RE^{3+} lattice sites were filled randomly with Yb^{3+} or Y^{3+} by a specified Yb-to-Y ratio. Substitution of one RE^{3+} ion by Tb^{3+} generated a particular configuration.

For each configuration (i.e., distribution around the Tb^{3+} ion) its single exponential decay signal $I(t)$ is given by

$$I(t) = \exp[-t(\gamma_{\mathrm{tr}} + \gamma_r)], \tag{11}$$

where t is time, γ_r is the radiative decay rate of the $^5D_4$ state of Tb^{3+} in YPO_4, and γ_{tr} is the energy-transfer rate. The signal measured in an experiment consists of luminescence

from an ensemble of Tb^{3+} ions. Therefore an ensemble-averaged signal is calculated in the Monte Carlo simulations,

$$\langle I(t)\rangle = \langle \exp[-t(\gamma_{\mathrm{tr}} + \gamma_r)]\rangle, \tag{12}$$

where $\langle\ \rangle$ denotes ensemble averaging over 10 000 configurations. With this number of configurations convergence was reached.

For a particular configuration the cooperative, accretive, and phonon-assisted energy-transfer rates were calculated according to

$$\text{Cooperative:} \quad \gamma_{\mathrm{tr}} = c_a \sum_i \sum_{j>i} \frac{1}{r_{i\mathrm{Tb}}^{2p} r_{j\mathrm{Tb}}^{2p}}, \tag{13a}$$

$$\text{Accretive:} \quad \gamma_{\mathrm{tr}} = c_b \sum_i \sum_{j>i} \left(\frac{1}{r_{i\mathrm{Tb}}^{2p} r_{ij}^{2p}} + \frac{1}{r_{j\mathrm{Tb}}^{2p} r_{ij}^{2p}} \right), \tag{13b}$$

$$\text{Phonon-assisted:} \quad \gamma_{\mathrm{tr}} = c_c \sum_i \frac{1}{r_{i\mathrm{Tb}}^{2p}}, \tag{13c}$$

where summation indices i and j refer to all Yb^{3+} ions in the lattice. The distance between ion i and j is given by $\mathbf{r}_{ij}$. The two parameters in Eqs. (13) are a proportionality constant c_i and the parameter p which determines the distance dependence of the interaction. For instance, for a dipole-dipole type of interaction $p=3$, which converts Eqs. (13a)–(13c) into Eqs. (7), (8), and (10), respectively.

Two types of simulations were performed. In the first one the distance dependence was fixed at $p=3$. In order to study a particular energy-transfer model i, c_i was obtained by subtracting the decay rate of the Tb^{3+} luminescence in YPO_4 (γ_r) from the decay rate of the Tb^{3+} luminescence in $YbPO_4$. This gives γ_{tr}. The lattice sums in Eqs. (13) are the same for all Tb^{3+} ions in $YbPO_4$. Equations (13) are then solved, yielding c_i. When c_i and p are known, γ_{tr} can be calculated for any configuration. Ensemble averaged decay curves were calculated for concentrations of Yb^{3+} ranging from 15 to 99%.

A second type of simulation was used to study the distance dependence of the energy-transfer processes. Here, in order to study a particular energy-transfer model i, the values of c_i and p were varied and ensemble averaged decay curves were computed for Yb^{3+} concentrations of 99, 75, 50, and 25%. The function H, which gives the squared deviation on a log scale for the computed curves to the experimental data, was defined to compare the simulated curves with experiments,

$$H = \sum_x \sum_{y(x)} [\ln(I_{xy}) - \ln(S_{xy})]^2. \tag{14}$$

Here, x denotes the concentration of Yb^{3+} ions and y stands for a specific data point. I and S denote the experimental and the simulated signal, respectively. Starting from an initial value of c_i and p (with a computed set of decay curves and value for H), a new guess for c_i and p resulted in a new set of decay curves and a new value for H. If this value decreased for the new c_i and p, the new parameters were approved. This iterative process was continued until convergence was reached.

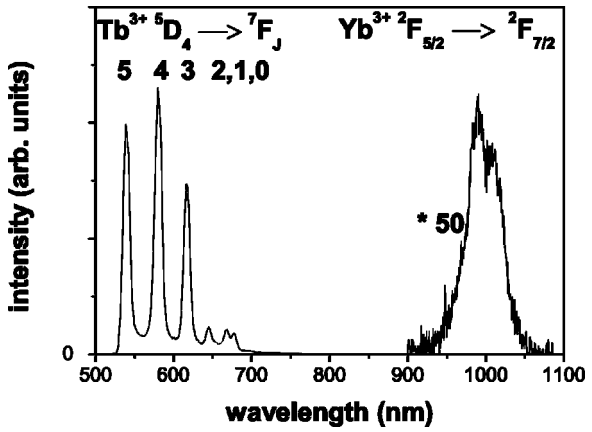

FIG. 3. Visible/near infrared emission spectrum of $Y_{0.74}Yb_{0.25}Tb_{0.01}PO_4$ upon $Tb^{3+}\,{}^7F_6 \rightarrow {}^5D_4$ excitation (489 nm). The spectral region between 900 and 1100 nm is amplified by a factor of 50.

D. Analytical solutions

Decay curves for the cooperative model were also calculated analytically. The procedure was the same as for the first type of Monte Carlo simulations, except that the probability distribution of the Yb^{3+} ions was calculated. For a cooperative process this is relatively straightforward since Tb^{3+} serves two times as the donor of energy. Thus the number of Yb^{3+} ions as a function of Tb–Yb distance determines the configuration. The probability P_{conf} for a particular configuration was calculated according to

$$P_{\mathrm{conf}} = \prod_{sh} \frac{N_{sh}!}{(N_{sh} - n_{\mathrm{Yb}})! n_{\mathrm{Yb}}!} c_{\mathrm{Yb}}^{n_{\mathrm{Yb}}} (1 - c_{\mathrm{Yb}})^{N_{sh} - n_{\mathrm{Yb}}}. \tag{15}$$

In Eq. (15) the product runs over all shells (as defined by RE-RE peaks in a radial distribution function) surrounding the Tb^{3+} ion. Product elements are elements of a binomial distribution function. c_{Yb} is the fraction of Yb^{3+} ions, N_{sh} is the number of RE sites in the shell and n_{Yb} is the number of Yb^{3+} ions in this shell for this particular configuration.

IV. RESULTS AND DISCUSSION

To investigate whether energy transfer from Tb^{3+} to Yb^{3+} occurs, an emission spectrum upon excitation in the $Tb^{3+}\,{}^5D_4$ level was recorded. Figure 3 shows the emission spectrum of $Yb_{0.25}Y_{0.74}Tb_{0.01}PO_4$ at room temperature upon $Tb^{3+}\,{}^7F_6 \rightarrow {}^5D_4$ excitation. In the region of 500–700 nm a series of lines is observed while in the 900–1100 nm region an emission band of much lower intensity appears (multiplied 50 times in Fig. 3). The lines in the visible part of the spectrum are due to $Tb^{3+}\,{}^5D_4 \rightarrow {}^7F_j$ multiplet emissions. They are similar to previous measurements on YPO_4 doped with Tb^{3+}.[35] Transitions to different ground state terms with J ranging from 5 to 0 are clearly resolved in the spectrum. The $Tb^{3+}\,{}^5D_4 \rightarrow {}^7F_6$ emission line is absent because of the use of

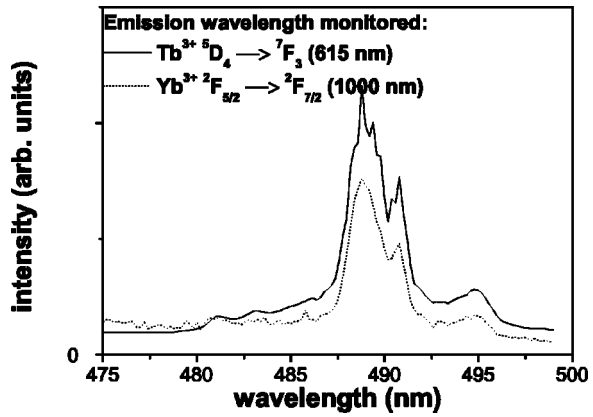

FIG. 4. Excitation spectra of the $Tb^{3+}\,{}^5D_4 \rightarrow {}^7F_3$ emission (615 nm, solid line) and the $Yb^{3+}\,{}^2F_{5/2} \rightarrow {}^2F_{7/2}$ emission (1000 nm, dotted line) in $Y_{0.74}Yb_{0.25}Tb_{0.01}PO_4$.

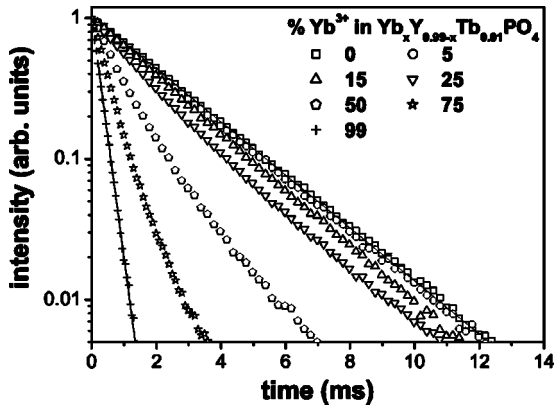

FIG. 5. Time-resolved signals of the $Tb^{3+}\,{}^5D_4 \rightarrow {}^7F_4$ luminescence (excitation wavelength = 489.6 nm, emission wavelength = 544.0 nm) for $Yb_xY_{0.99-x}Tb_{0.01}PO_4$. Every tenth data-point is shown. The different fractions x of Yb^{3+} in the $Yb_xY_{0.99-x}Tb_{0.01}PO_4$ samples are indicated in the figure. Solid lines are single exponential fits.

a 540 nm cutoff filter. This filter was used to prevent second order Tb^{3+} emissions in the wavelength region of 900–1100 nm, since these emissions would obscure the detection of Yb^{3+} emission lines. The features in this part of the spectrum are attributed to the $Yb^{3+}\,{}^2F_{5/2} \rightarrow {}^2F_{7/2}$ transitions. The comparatively large linewidth of the Yb^{3+} emissions is probably due to the relatively long wavelengths involved, giving larger width on a wavelength scale for the same width on an energy scale, and the strong electron-phonon coupling of Yb^{3+} ions,[36] giving pronounced phonon-induced line broadening.

Compared to the Tb^{3+} emission, the intensity of the Yb^{3+} luminescence is weak. This may be due to three reasons. First, the response of the grating and the detector are not optimal in the IR region, leading to a reduced signal of a factor of ~15. Second, concentration quenching (the migration of excitation energy over Yb^{3+} ions to quenching sites) reduces the luminescence quantum yield for a doping concentration of 25%. Third, only a small fraction of the Yb^{3+} ions are excited. Although with 25% Yb^{3+} doping concentration two or more Yb^{3+} ions are expected to be at close range to a Tb^{3+} ion, an energy-transfer process competes with radiative depopulation of the $Tb^{3+}\,{}^5D_4$ level. To maximize the luminescence output of the Yb^{3+} ions upon excitation in the Tb^{3+} $4f^8$ levels, one has to consider competition between the energy-transfer efficiency (increasing the Yb^{3+} emission intensity for higher Yb^{3+} concentration) and concentration quenching (decreasing the Yb^{3+} luminescence intensity for higher Yb^{3+} concentration). A 25% doping concentration gave the highest Yb^{3+} emission intensity.

Excitation spectra of Tb^{3+} and Yb^{3+} emissions in $Yb_{0.25}Y_{0.74}Tb_{0.01}PO_4$ were recorded to give convincing evidence for the presence of $Tb^{3+} \rightarrow Yb^{3+}$ energy transfer. Figure 4 shows the wavelength region where the $Tb^{3+}\,{}^7F_6 \rightarrow {}^5D_4$ transition is located.[37,38] The solid line depicts the excitation spectrum of the $Tb^{3+}\,{}^5D_4 \rightarrow {}^7F_3$ emission. The dotted line shows the excitation spectrum of the $Yb^{3+}\,{}^2F_{5/2} \rightarrow {}^2F_{7/2}$ emission. In both spectra lines are located around 485–495 nm. For the spectrum monitoring the $Tb^{3+}\,{}^5D_4 \rightarrow {}^7F_3$ emission, the excitation lines are assigned to the well-known $^7F_6 \rightarrow {}^5D_4$ transitions. This absorption was also detected in previous experiments of YPO_4 doped with Tb^{3+}.[35] The excitation spectrum when monitoring the Yb^{3+} emission is very similar to the $Tb^{3+}\,{}^5D_4 \rightarrow {}^7F_3$ excitation spectrum. The observation of the $Tb^{3+}\,{}^7F_6 \rightarrow {}^5D_4$ lines in the excitation spectrum of Yb^{3+} shows that energy transfer from Tb^{3+} to Yb^{3+} is present. No sign of RE impurities (typically present in concentrations lower than 0.01%) was observed in either the emission or excitation spectra.

Now that the occurrence of $Tb^{3+} \rightarrow Yb^{3+}$ energy transfer has been established, it is interesting to investigate the mechanism and efficiency of the energy-transfer process. The Dieke diagrams of Tb^{3+} and Yb^{3+} (Refs. 37 and 38) show that only a second-order energy-transfer process can occur between the $Tb^{3+}\,{}^5D_4 \rightarrow {}^7F_J$ and the $Yb^{3+}\,{}^2F_{5/2} \rightarrow {}^2F_{7/2}$ transitions. Resonant energy transfer from the $^5D_4$ state of Tb^{3+} to one Yb^{3+} is not possible since the Yb^{3+} ion has only one excited multiplet ($^2F_{5/2}$) around 10 000 cm^{-1} and no transition from the $Tb^{3+}\,{}^5D_4$ level is situated at this energy. In addition, unwanted absorptions due to defect states, impurities, or Yb^{3+} pair states are absent in both excitation spectra and therefore alternative resonant energy-transfer processes do not interfere. An alternative for an energy-transfer process involving two Yb^{3+} ions is mentioned in the literature as phonon-assisted energy transfer.[20,22,23] On the basis of emission and excitation spectra this competing process cannot be excluded. Below we will show that by analyzing transient luminescence curves phonon-assisted energy transfer can be ruled out.

In Fig. 5 the decay curves of the $Tb^{3+}\,{}^5D_4 \rightarrow {}^7F_4$ luminescence (544.0 nm) are plotted for Yb^{3+} concentrations of 0, 5, 15, 25, 50, 75, and 99%. The Tb^{3+} emission in $YPO_4:Tb^{3+}$ 1% shows a nearly single exponential decay as expected (only radiative decay). A monoexponential fit yields a decay time of 2.3 ms. A decay time between 2 and 3 ms is a typical value compared to $Tb^{3+}\,{}^5D_4$ emission in oxides where the site of Tb^{3+} lacks inversion symmetry.[17,22,24,34] When the Yb^{3+} concentration is increased, the decay curve decreases more rapidly and it becomes nonexponential. For $YbPO_4:Tb^{3+}$ 1% the fastest decay is observed and the curve

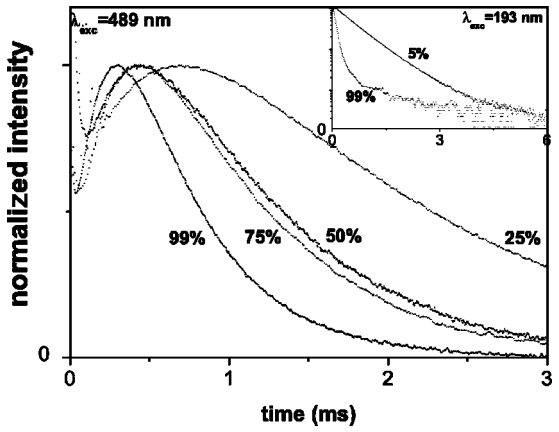

FIG. 6. Decay curves (RT) of the $Yb^{3+}\ {}^2F_{5/2} \rightarrow {}^2F_{7/2}$ luminescence as a function of Yb^{3+} concentration in $Yb_xY_{0.99-x}Tb_{0.01}PO_4$. The Yb^{3+} concentrations are indicated in the figure. The Yb^{3+} luminescence monitored in the main figure is after excitation in the $Tb^{3+}\ {}^5D_4$ level (489 nm). The Yb^{3+} luminescence monitored in the inset is after excitation into the Yb–O charge transfer band (193 nm).

is again nearly single exponential. The faster decline as a function of Yb^{3+} concentration can be explained by the introduction of extra decay pathways due to the Yb^{3+}-doping: energy transfer from $Tb^{3+}\ {}^5D_4$ to Yb^{3+} enhances the $Tb^{3+}\ {}^5D_4$ decay rate. The presence of Yb^{3+} ions also explains the nonexponential behavior at intermediate doping concentrations and the single exponential behavior for 99% Yb^{3+}. At intermediate doping concentrations the Yb^{3+} and the Y^{3+} ions are randomly distributed over the RE^{3+} lattice sites. Thus the environment of every Tb^{3+} ion is different, leading to a variety of transfer rates. At a Yb^{3+} fraction of 99% the Tb^{3+} ions are surrounded by Yb^{3+} ions only, leading to a single decay component. Therefore the 99% Yb^{3+} decay curve in Fig. 5 is again nearly single exponential. Fitting this curve with a single exponential function yields a decay time of 0.25 ms.

Assuming that the radiative rate of the $Tb^{3+}\ {}^5D_4$ emission does not change when Y^{3+} is substituted for Yb^{3+}, the energy-transfer rate in $YbPO_4$ can be calculated by subtracting the $Tb^{3+}\ {}^5D_4$ radiative decay rate from the decay rate in $YbPO_4$. This results in an energy-transfer rate of $3.5 \times 10^3\ s^{-1}$ in $YbPO_4$:Tb^{3+} 1%. This is roughly an order of magnitude faster than the radiative decay rate of Tb^{3+} and indicates that the energy-transfer process is efficient.

Figure 6 shows the time-resolved Yb^{3+} luminescence for different Yb^{3+} concentrations upon excitation into the $Tb^{3+}\ {}^5D_4$ level. The Yb^{3+} luminescence shows a rise that is caused by energy transfer from Tb^{3+} to Yb^{3+}. As the Yb^{3+} concentration increases, the rise becomes shorter. This is attributed to a faster depopulation of the Tb^{3+} donors due to the presence of more Yb^{3+} acceptors. For all samples the observed rise times are in good agreement with the decay times of the Tb^{3+} emission, confirming the feeding of the Yb^{3+} excited state by energy transfer from Tb^{3+} to Yb^{3+}. The inset shows the Yb^{3+} luminescence after excitation into the Yb–O charge-transfer (CT) band. Upon excitation in the CT state of Yb^{3+}, the ${}^2F_{5/2}$ state is populated directly and the

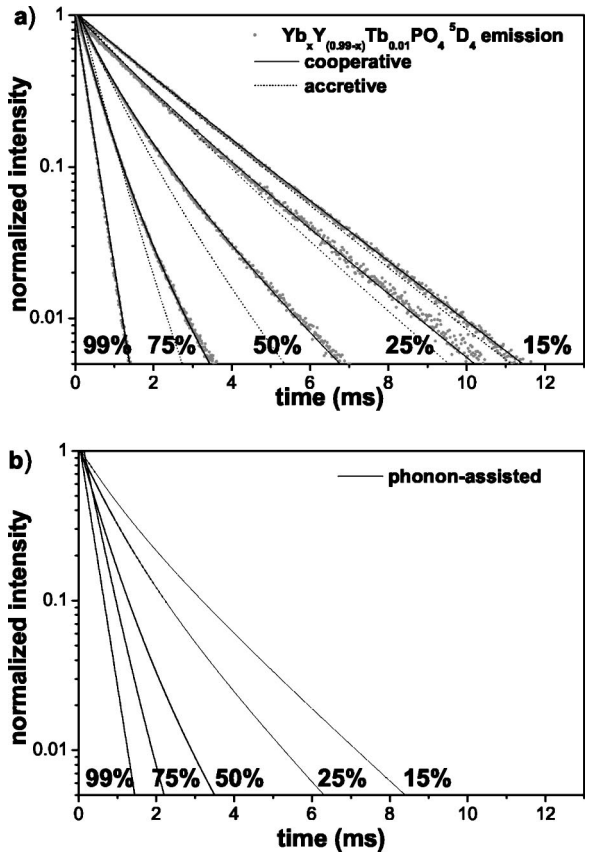

FIG. 7. (a) Luminescence decay curves of the $Tb^{3+}\ {}^5D_4$ emission for various concentrations of Yb^{3+} (see Fig. 5) replotted with simulation results. The dots are the experimental results. The solid lines are simulated curves using a cooperative dipole-dipole model [Eq. (13a)]. Dotted lines are simulated curves using an accretive dipole-dipole model [Eq. (13b)]. (b) Simulated decay curves for the phonon-assisted dipole-dipole model [Eq. (13c)]. For both figures the Yb^{3+} concentrations are indicated in the figure. The single exponential decay of the experimental data at 99% Yb^{3+} concentration is used to fit the parameter c_i in Eqs. (13).

lifetime of the ${}^2F_{5/2}$ emission can be measured without interference due to the feeding from Tb^{3+}. The Yb^{3+} luminescence of the $YbPO_4$:Tb^{3+} 1% sample shows a markedly faster decrease in intensity than the 5% doped sample: $\tau_{1/e} = 78\ \mu s$ in $YbPO_4$ and 610 μs in YPO_4:Tb^{3+} 1% Yb^{3+} 5%. The short luminescence lifetime in the concentrated sample confirms the presence of strong concentration quenching. This explains the low relative intensity of the Yb^{3+} emission in the luminescence spectra.

To distinguish between the three energy-transfer mechanisms (cooperative, accretive, and phonon-assisted) the donor decay curves were compared to the decay behavior predicted by Monte Carlo simulations. Experiments and simulated results for the cooperative, the accretive, and the phonon-assisted dipole-dipole ($p=3$) models are shown in Fig. 7. To obtain the computed curves, the radiative decay rate and the energy-transfer rate in $YbPO_4$ (as determined from single exponential fits to the decay curves of YPO_4 and $YbPO_4$ in Fig. 5) were used as input parameters. Therefore, at 99% Yb^{3+} concentration, the three simulated curves all

match the experimental curve. However, the cooperative model matches the experiments for all Yb^{3+} concentrations while the accretive and phonon-assisted energy-transfer models deviate substantially. At all intermediate Yb^{3+} concentrations, the decay profiles of the phonon-assisted model and the accretive model fall much faster than the cooperative model. This is consistent with the distance dependence in Eqs. (13) and the fitting of the c_i's. For intermediate Yb^{3+} concentrations, the phonon-assisted model yields a nonradiative decay channel for every Yb^{3+} ion present, resulting in a relatively fast increase of the decay rate as a function of Yb^{3+} concentration. The slowest increase of the decay rate as a function of the Yb^{3+} concentration is expected for second-order mechanisms, since these mechanisms require two Yb^{3+} ions in close proximity to a Tb^{3+} ion. For every combination of two Yb^{3+} and one Tb^{3+}, the cooperative mechanism has one pathway where the accretive mechanism has two pathways. The relative importance of the pathways to the decay rate is not equal. The $1/r^{2p}$ distance dependence favors the shortest pathway, so that the accretive model falls faster than the cooperative model. The experimental results clearly show that energy transfer by a cooperative mechanism is the dominant process.

In our analysis the possibility of upconversion was neglected. This is justified since at doping concentrations higher than ~10% energy migration to the different Yb^{3+} sites will suppress the upconversion process: after energy transfer from Tb^{3+} to two Yb^{3+} ions the situation of two excited Yb^{3+} ions close to Tb^{3+} will be eliminated by fast energy migration over the Yb^{3+} ions.

The dipole-dipole nature of the energy-transfer mechanisms was tested by varying p (and c_i), i.e., by using the second type of Monte Carlo simulations described in the Experiment section. For the cooperative model the minimum of H, Eq. (14), was reached for $p=3.1$ and $c_a=2.05\times10^9$ Å^{12} s^{-1}. This results in an energy-transfer rate to two Yb^{3+} ions at nearest-neighbor (NN) distance of 260 s^{-1}. The value obtained for p confirms the dipole-dipole nature of the energy-transfer mechanism. For the accretive and phonon-assisted model the value of H was much larger for any p between 2 and 5, thus ruling out those models.

We also investigated the relative contribution of the different models by fitting the decay curves $[I(t)]$ at different Yb^{3+} concentrations simultaneously using

$$I(t) = (1-x-y)I_{\text{coop}}(t,c_a,p_a) + xI_{\text{accr}}(t,c_b,p_b) + yI_{\text{pa}}(t,c_c,p_c) \tag{16}$$

in which x and y are the relative contribution of the accretive and phonon-assisted model. As we have fixed $p_a=3$ for the cooperative model, our model includes seven fitting parameters $(c_a,c_b,c_c,p_b,p_c,x,y)$ in which p_b and p_c could be either 3, 4, or 5. It turns out that this procedure yields $x<10^{-3}$ and $y<10^{-3}$, which clearly demonstrates that the cooperative mechanism is dominant.

The value for γ_{tr} to two Yb^{3+} nearest neighbors of 260 s^{-1} is similar to values for the cooperative transfer rates reported by Basiev *et al.*[10] The transfer rates for this second order process are a factor of 10^4 to 10^8 times smaller then typical values reported for first-order energy-transfer rates involving nearest neighbors for which values range between 10^7 and 10^{11} s^{-1}.[39–41]

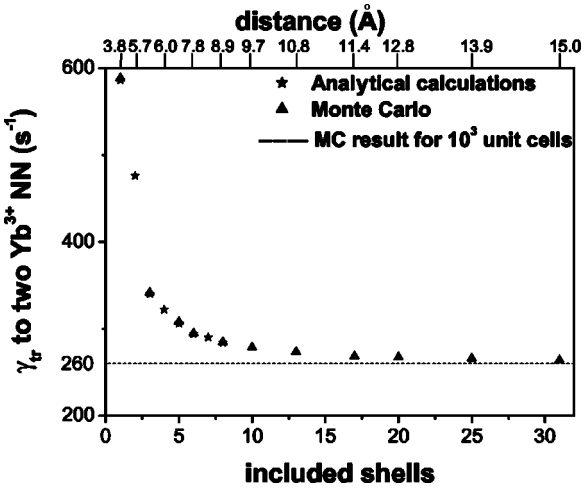

FIG. 8. The cooperative transfer rate to two Yb^{3+} nearest neighbors (NN) as a function of the number of shells included in the simulations and calculations. The stars represent analytical calculations and the triangles depict the Monte Carlo simulations. The dashed line represents the value obtained from Monte Carlo simulations for a box size of 10^3 unit cells.

Analytical calculations including up to eight shells (comparable to a box size of 3^3 in the Monte Carlo simulations) have been performed for the cooperative mechanism. To obtain information about the convergence distance of the energy-transfer process the transfer rate to two nearest-neighbor Yb^{3+} ions, as obtained by fitting to the decay curve of the Tb^{3+} luminescence in $YbPO_4$:Tb^{3+} 1%, is plotted as a function of included shells in Fig. 8. Here, the stars and triangles represent, respectively, the calculated and simulated energy-transfer rate to two nearest-neighbor Yb^{3+} ions when a particular number of shells is included in the calculation. The trend in the data is as expected: when few shells are included, the transfer rate to Yb pairs is overestimated due to the neglect of the contribution to the transfer rate from longer distance Yb^{3+} ions. When more shells are included, the transfer rate levels off to the Monte Carlo result for 10^3 boxes (dashed horizontal line in Fig. 8). As is seen from the figure, about 90% of the transfer processes take place within a distance of eight shells (8.9 Å). A box size of 5^3 unit cells corresponds to 31 shells. At this point the energy-transfer rate has reached 265 s^{-1}, which is only 2% larger than the value for 10^3 unit cells (260 s^{-1}). Furthermore, the agreement between analytical calculation and simulation is excellent.

From the luminescence decay curves in Fig. 5 the energy-transfer efficiency and the quantum efficiency can be determined. The energy-transfer efficiency $\eta_{\text{tr,x\%Yb}}$ is defined as the ratio of Tb^{3+} ions that depopulate by energy transfer to Yb^{3+} ions over the total number of Tb^{3+} ions excited. We define the total quantum efficiency, $\eta_{\text{x\%Yb}}$, as the ratio of the

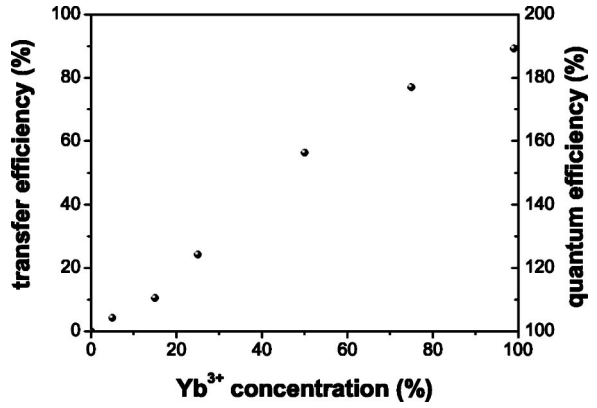

FIG. 9. Transfer efficiency [Eq. (17)] and quantum efficiency [Eq. (18)] as a function of the Yb^{3+} concentration in $Yb_xY_{0.99-x}Tb_{0.01}PO_4$.

number of photons emitted (visible and infrared) to the number of photons absorbed, assuming that all excited Yb^{3+} ions decay radiatively. This assumption leads to an upper limit of the quantum efficiency. The actual quantum efficiency is lower due to concentration quenching. By dividing the integrated intensity of the decay curves of the $Yb_xY_{0.99-x}Tb_{0.01}PO_4$ samples to the integrated intensity of the $YPO_4:Tb^{3+}$ 1% curve the transfer efficiency is obtained as a function of the Yb^{3+} concentration,

$$\eta_{\mathrm{tr,x\%Yb}} = 1 - \frac{\int I_{\mathrm{x\%Yb}}dt}{\int I_{\mathrm{0\%Yb}}dt}, \tag{17}$$

where I denotes intensity and $x\%\mathrm{Yb}$ stands for the Yb^{3+} concentration. The relation between the transfer efficiency and the total quantum efficiency is linear and defined as

$$\eta_{\mathrm{x\%Yb}} = \eta_{\mathrm{rTb}}(1 - \eta_{\mathrm{tr,x\%Yb}}) + 2\,\eta_{\mathrm{tr,x\%Yb}}, \tag{18}$$

where the quantum efficiency for the Tb^{3+} ions, η_{rTb}, is also set to 1.

In Fig. 9 the transfer efficiency and the quantum efficiency are plotted versus Yb^{3+} concentration. When the Yb^{3+} concentration is increased, the transfer efficiency shows an increase up to a maximum value of 88% in $YbPO_4:Tb^{3+}$ 1%. For this sample the transfer efficiency may also be obtained using the fitted decay rates of $YPO_4:Tb^{3+}$ 1% and $YbPO_4:Tb^{3+}$ 1%, yielding the same value. For $YbPO_4:Tb^{3+}$ 1% a quantum efficiency of 188% is obtained. This means that depopulation of the Tb^{3+} $^5D_4$ level proceeds 88 out of 100 times by excitation of two Yb^{3+} ions to the $^2F_{5/2}$ level. A quantum efficiency of 188% is close to the limit of 200% and comparable to the most efficient downconversion process known.[1]

The high efficiency of the energy transfer may seem surprising since it involves a second-order energy-transfer process. The factors contributing to this high value are, first, the low probability of competitive processes: the excited state of the donor has a long lifetime and first-order energy transfer is absent. Second, the cooperative transfer rate should be high. According to Eqs. (1)–(3) the atomic parameters that determine the cooperative energy-transfer rate are the transition dipole moments of the acceptors, the transition dipole moments of the donor, the energetic location of the virtual states, and the spectral overlap integral. The proximity (in energy) and the large transition dipole moments of the fully allowed Tb^{3+} $4f^8 \rightarrow 4f^7 5d$ transitions enhance the cooperative energy-transfer rate. Furthermore, the energetic positions of the Yb^{3+} energy levels compared to the Tb^{3+} $^5D_4$ excited state provide a good spectral overlap for second-order energy transfer.

Materials exploiting Tb–Yb cooperative quantum cutting may increase the efficiency of silicon-based solar cells by downconverting the green-to-UV part of the solar spectrum to ~1000 nm photons, with almost complete doubling of the number of photons. The weak IR emission of the presently studied materials (see Fig. 3) shows that, although the physics of the energy-transfer process allow for efficient quantum cutting, the actual quantum efficiency in the IR is still low. In order to obtain a material with an actual quantum efficiency close to 200%, two drawbacks should be overcome. First, due to the high Yb^{3+} concentration needed for efficient downconversion, concentration quenching of the Yb^{3+} emission is a major issue. To overcome this problem, incorporation of ions with an excited state at slightly lower energy than the $^2F_{5/2}$ state of the Yb^{3+} ion (but still higher than the band gap of crystalline Si) may be used. These ions will function as traps for the energy in the $^2F_{5/2}$ state so that migration of excitation energy to quenching sites is suppressed. Another possibility is the use of one-dimensional systems in order to localize the energy migration.[42–44] The second obstacle is the low absorption cross section for green-to-UV light of Yb/YPO_4 doped with Tb^{3+}. The absorption cross section may be enhanced in two ways. First, a bulk material with a lower band gap may be used so that the host itself would absorb part of the solar spectrum, after which energy transfer to a Tb^{3+} ion should occur. Second, sensitizer ions could be used to absorb the desired part of the solar spectrum and transfer the excitation energy to the $^5D_4$ state of Tb^{3+} for the Tb–Yb downconversion process.

V. CONCLUSION

In this paper experimental evidence is presented for cooperative energy transfer in $Yb_xY_{1-x}PO_4:Tb^{3+}$. Emission, excitation, and time-resolved luminescence measurements show the occurrence of energy transfer from the $^5D_4$ level of Tb^{3+} (around 20 000 cm^{-1}) to two Yb^{3+} ions, exciting both ions from the $^2F_{7/2}$ ground state to the $^2F_{5/2}$ excited state around 10 000 cm^{-1}. Monte Carlo simulations of the luminescence decay curves are a useful tool for the determination of the energy-transfer mechanism. Under the assumption of cooperative dipole-dipole interaction, the simulated and the experimental luminescence decay curves are in excellent agreement for all Yb^{3+} concentrations. On the basis of the very poor agreement between simulation and experiment it is possible to exclude energy transfer via an accretive dipole-dipole mechanism or a phonon-assisted energy-transfer process.

In $(Y,Yb)PO_4:Tb^{3+}$ 1%, the cooperative energy-transfer rate to a pair of nearest-neighbor Yb^{3+} ions is 0.26 ms^{-1}. The corresponding efficiency of the quantum cutting process is 88% in $YbPO_4:Tb^{3+}$ 1%. This yields an upper limit for the quantum efficiency (VIS+IR) of 188%, but the actual quantum efficiency is strongly reduced by concentration quenching of the IR emission from Yb^{3+}. High concentrations of Yb^{3+} are needed for efficient cooperative energy transfer from Tb^{3+} to 2 Yb^{3+}. To develop a commercially interesting material, for example, for photon doubling in silicon solar cells, solutions need to be found for concentration quenching of the Yb^{3+} $^2F_{5/2}\rightarrow{}^2F_{7/2}$ emission and also for the low absorption cross section of $(Y,Yb)PO_4:Tb^{3+}$ 1% in the green-to-UV region.

A transfer efficiency of 88% is a surprisingly high number for a second-order energy-transfer process. A long lifetime of the excited state of the donor, the absence of first-order energy transfer, the energetically close location of allowed transitions on the donor, and a good spectral overlap for second-order energy-transfer processes can explain this high efficiency. For other compounds which meet these criteria, cooperative energy transfer may be used to obtain efficient quantum cutting as well.

ACKNOWLEDGMENTS

The authors are grateful to H. W. de Wijn and M. Gießelbach for helpful discussions. F. Suyver (University of Bern, Switzerland) is acknowledged for fruitful discussions and useful measurements. The work described here was supported by the Council for Chemical Sciences (CW), with financial aid from the Netherlands Foundation for Technical Research (STW).

*Author to whom correspondence should be addressed. FAX: +31 30 2532403. Email address: p.vergeer@phys.uu.nl

[1] R. T. Wegh, H. Donker, K. D. Oskam, and A. Meijerink, Science **283**, 663 (1999).
[2] R. T. Wegh, E. V. D. van Loef, and A. Meijerink, J. Lumin. **90**, 111 (2000).
[3] T. Trupke, M. A. Green, and P. Wurfel, J. Appl. Phys. **92**, 1668 (2002).
[4] W. W. Piper, J. A. DeLuca, and F. S. Ham, J. Lumin. **8**, 344 (1974).
[5] J. L. Sommerdijk, A. Bril, and A. W. de Jager, J. Lumin. **9**, 288 (1974).
[6] R. Pappalardo, J. Lumin. **14**, 159 (1976).
[7] R. T. Wegh, H. Donker, A. Meijerink, R. J. Lamminmaki, and J. Holsa, Phys. Rev. B **56**, 13841 (1997).
[8] T. Forster, Ann. Phys. **2**, 55 (1948).
[9] D. L. Dexter, Phys. Rev. **108**, 630 (1957).
[10] T. T. Basiev, M. E. Doroshenko, and V. V. Osiko, JETP Lett. **71**, 8 (2000).
[11] T. T. Basiev, I. T. Basieva, M. E. Doroshenko, V. V. Osiko, A. M. Prokhorov, and K. K. Pukhov, J. Lumin. **94**, 349 (2001).
[12] I. T. Basieva, K. K. Pukhov, and T. T. Basiev, JETP Lett. **74**, 539 (2001).
[13] L. D. Livanova, I. G. Saitkulov, and A. L. Stolov, Sov. Phys. Solid State **11**, 750 (1969).
[14] F. W. Ostermayer, Jr. and L. G. Van Uitert, Phys. Rev. B **1**, 4208 (1970).
[15] B. M. Antipenko, A. V. Dmitryuk, G. O. Karapetyan, V. S. Zubkova, V. I. Kosyakov, A. A. Mak, and N. V. Mikhailova, Opt. Spectrosc. **35**, 540 (1973).
[16] F. Auzel, J. Lumin. **45**, 341 (1990).
[17] R. S. Brown, W. S. Brocklesby, W. L. Barnes, and J. E. Townsend, J. Lumin. **63**, 1 (1995).
[18] M. A. Noginov, P. Venkateswarlu, and M. Mahdi, J. Opt. Soc. Am. B **13**, 735 (1996).
[19] J. L. Adam, N. Duhamel-Henry, and J. Y. Allain, J. Non-Cryst. Solids **213&214**, 245 (1997).
[20] W. Strek, P. Deren, and A. Bednarkiewicz, J. Lumin. **87-9**, 999 (2000).
[21] G. M. Salley, R. Valiente, and H. U. Guedel, J. Lumin. **94**, 305 (2001).
[22] I. R. Martin, A. C. Yanes, J. Mendez-Ramos, M. E. Torres, and V. D. Rodriguez, J. Appl. Phys. **89**, 2520 (2001).
[23] W. Strek, A. Bednarkiewicz, and P. J. Deren, J. Lumin. **92**, 229 (2001).
[24] G. M. Salley, R. Valiente, and H. U. Gudel, J. Phys. A **14**, 5461 (2002).
[25] G. M. Salley, R. Valiente, and H. U. Gudel, Phys. Rev. B **67**, 134111 (2003).
[26] T. Miyakawa and D. L. Dexter, Phys. Rev. B **1**, 2961 (1970).
[27] D. L. Andrews and R. D. Jenkins, J. Chem. Phys. **114**, 1089 (2001).
[28] B. Henderson and G. F. Imbusch, *Optical Spectroscopy of Inorganic Solids* (Oxford University Press, New York, 1989).
[29] C. de Mello Donega, A. Meijerink, and G. Blasse, J. Phys. A **4**, 8889 (1992).
[30] O. Barbosa-Garcia and C. W. Struck, J. Chem. Phys. **100**, 4554 (1994).
[31] J. T. Vega-Duran, O. Barbosa-Garcia, L. A. Diaz-Torres, M. A. Meneses-Nava, and D. S. Sumida, Appl. Phys. Lett. **76**, 2032 (2000).
[32] J. T. Vega-Duran, L. A. Diaz-Torres, M. A. Meneses-Nava, J. L. Maldonado-Rivera, and O. Barbosa-Garcia, J. Phys. D **34**, 3203 (2001).
[33] W. O. Milligan, D. F. Mullica, G. W. Beall, and L. A. Boatner, Inorg. Chim. Acta **60**, 39 (1982).
[34] P. C. Becker, T. Hayhurst, G. Shalimoff, J. G. Conway, N. Edelstein, L. A. Boatner, and M. M. Abraham, J. Chem. Phys. **81**, 2872 (1984).
[35] R. C. Ropp, J. Electrochem. Soc. **115**, 841 (1968).
[36] P. C. Becker, G. M. Williams, N. M. Edelstein, J. A. Koningstein, L. A. Boatner, and M. M. Abraham, Phys. Rev. B **45**, 5027 (1992).
[37] G. H. Dieke, *Spectra and Energy Levels of Rare Earth Ions in Crystals* (Interscience, New York, 1968).
[38] G. H. Dieke and H. M. Crosswhite, Appl. Opt. **2**, 675 (1963).

[39] C. Barthou and R. B. Barthem, J. Lumin. **46**, 9 (1990).
[40] R. Mahiou, B. Jacquier, and C. Madej, J. Chem. Phys. **89**, 5931 (1988).
[41] J. Hegarty, D. L. Huber, and W. M. Yen, Phys. Rev. B **25**, 5638 (1982).
[42] M. Buijs and G. Blasse, J. Lumin. **34**, 263 (1986).
[43] M. Buijs, J. I. Vree, and G. Blasse, Chem. Phys. Lett. **137**, 381 (1987).
[44] M. Buijs and G. Blasse, J. Lumin. **39**, 323 (1988).